

## Article

# Chemical Compatibility and Electrochemical Performance of Ba<sub>7</sub>Ta<sub>3.7</sub>Mo<sub>1.3</sub>O<sub>20.15</sub> Electrolytes for Solid Oxide Fuel Cells

Dong Xu, Xingkai Zhou, Yu Li, Xiaole Yu, Zhexiang Yu, Bochang Shi, Yaowei Mi, Bangze Wu and Lin Ge \*

College of Materials Science and Engineering, Nanjing Tech University, No. 30 South Puzhu Road, Nanjing 211816, China; 202061103074@njtech.edu.cn (D.X.); 202161203206@njtech.edu.cn (X.Z.); 202061103073@njtech.edu.cn (Y.L.); yxl0908@njtech.edu.cn (X.Y.); 202061103052@njtech.edu.cn (Z.Y.); 202161203149@njtech.edu.cn (B.S.); 202161103123@njtech.edu.cn (Y.M.); 202261203315@njtech.edu.cn (B.W.)

\* Correspondence: gelin2013@njtech.edu.cn

**Abstract:** Hexagonal perovskite-related oxides Ba<sub>7</sub>Ta<sub>3.7</sub>Mo<sub>1.3</sub>O<sub>20.15</sub> (BTM) have recently been reported as promising electrolyte materials for intermediate-temperature solid oxide fuel cells (IT-SOFCs). In this work, sintering properties, thermal expansion coefficient, and chemical stability of BTM were studied. In particular, the chemical compatibilities of (La<sub>0.75</sub>Sr<sub>0.25</sub>)<sub>0.95</sub>MnO<sub>3±δ</sub> (LSM), La<sub>0.6</sub>Sr<sub>0.4</sub>CoO<sub>3</sub> (LSC), La<sub>0.6</sub>Sr<sub>0.4</sub>Co<sub>0.2</sub>Fe<sub>0.8</sub>O<sub>3+δ</sub> (LSCF), PrBaMn<sub>2</sub>O<sub>5+δ</sub> (PBM), Sr<sub>2</sub>Fe<sub>1.5</sub>Mo<sub>0.5</sub>O<sub>6-δ</sub> (SFM), BaCo<sub>0.4</sub>Fe<sub>0.4</sub>Zr<sub>0.1</sub>Y<sub>0.1</sub>O<sub>3-δ</sub> (BCFZY), and NiO electrode materials with the BTM electrolyte were evaluated. The results show that BTM is highly reactive with these electrodes, in particular, BTM tends to react with Ni, Co, Fe, Mn, Pr, Sr, and La elements in the electrodes to form resistive phases, thus deteriorating the electrochemical properties, which has not been reported before.

**Keywords:** solid oxide fuel cell (SOFC); hexagonal perovskite electrolyte; chemical compatibility; cathode materials



**Citation:** Xu, D.; Zhou, X.; Li, Y.; Yu, X.; Yu, Z.; Shi, B.; Mi, Y.; Wu, B.; Ge, L. Chemical Compatibility and Electrochemical Performance of Ba<sub>7</sub>Ta<sub>3.7</sub>Mo<sub>1.3</sub>O<sub>20.15</sub> Electrolytes for Solid Oxide Fuel Cells. *Materials* **2023**, *16*, 3919. <https://doi.org/10.3390/ma16113919>

Academic Editor: Alessandro Dell'Erà

Received: 13 April 2023

Revised: 13 May 2023

Accepted: 19 May 2023

Published: 23 May 2023



**Copyright:** © 2023 by the authors. Licensee MDPI, Basel, Switzerland. This article is an open access article distributed under the terms and conditions of the Creative Commons Attribution (CC BY) license (<https://creativecommons.org/licenses/by/4.0/>).

## 1. Introduction

Solid oxide fuel cells (SOFCs) have attracted much attention as sustainable energy-conversion devices for their high-energy conversion efficiency, fuel flexibility, and environmental friendliness [1]. The electrolyte has been extensively investigated due to its function of connecting the cathode to the anode and conducting ions. Since the operating temperature of Yttria stabilized zirconia (YSZ) is above 700 °C [2], affecting the practical application of the battery, it is necessary to search for an electrolyte that can operate at intermediate temperatures (300–600 °C) with sufficiently high ionic conductivity. Extensive research on crystal structures has led to the discovery of various electrolyte materials with different structures such as the fluorite-type [3–5], perovskite-type [6–10], melilite-type [11], and apatite-type [12] structures, that exhibit high ionic conductivity at intermediate temperatures.

Amongst these crystal structures, the perovskite-type structure shows great potential for both oxygen ion conduction and proton conduction due to its flexible framework that can accommodate a variety of cations and its flexible coordination environment that can stabilize oxygen vacancies [13–15]. For instance, La<sub>x</sub>Sr<sub>1-x</sub>Ga<sub>1-y</sub>Mg<sub>y</sub>O<sub>3</sub> (LSGM) exhibits high oxygen ionic conductivity at intermediate temperatures, and doped BaCeO<sub>3</sub> and BaZrO<sub>3</sub> showed excellent proton conduction below 600 °C [16–19].

Recently, the hexagonal perovskite material Ba<sub>7</sub>Nb<sub>4</sub>MoO<sub>20</sub> was reported to exhibit high ionic conductivity due to its unique disordered structure [20]. Hexagonal perovskite-related structures are composed of hexagonal close-packed AO<sub>3</sub> (h) layers or sequences of hexagonal and cubic close-packed AO<sub>3</sub> (c) layers (and anion-deficient AO<sub>3-x</sub> (c')) where x is the anion vacancy concentration). The disordered stacking of (h) and (c) layers results in the formation of BO<sub>6</sub> octahedra with face-sharing and corner-sharing [21]. This structure allows the doping of different metal cations to form oxygen vacancies, thus enabling ion

transport. Yashima M et al. [22] changed the ratio of cations and thus allowed for the introduction of interstitial oxygen in the (c') layer, which greatly improved the ionic conductivity of the electrolyte, reaching  $5.8 \times 10^{-4} \text{ S cm}^{-1}$  for  $\text{Ba}_7\text{Nb}_{3.9}\text{Mo}_{1.1}\text{O}_{20.05}$  at 310 °C. Suzuki Y et al. [23] introduced a portion of  $\text{W}^{6+}$  in the (c') layer in place of  $\text{Nb}^{5+}$ , which greatly improved the conductivity of  $\text{Ba}_7\text{Nb}_{3.85}\text{W}_{0.15}\text{MoO}_{20.075}$ , reaching  $2.2 \times 10^{-2} \text{ S cm}^{-1}$  at 600 °C. Taito Murakami et al. [24] prepared  $\text{Ba}_7\text{Ta}_{3.7}\text{Mo}_{1.3}\text{O}_{20.15}$  (BTM) by replacing  $\text{Nb}^{5+}$  with  $\text{Ta}^{5+}$ , introduced more interstitial oxygen, with high oxygen ion conduction and only a small amount of electron conductivity, and the conductivity reached  $1.08 \times 10^{-3} \text{ S cm}^{-1}$  at 377 °C.

Therefore, BTM is a promising electrolyte material for SOFC. However, to the best of our knowledge, there is no research available that investigates the chemical compatibility between BTM and electrode materials. During preparation and operation, chemical reactions occur to form new phases due to poor chemical compatibility between materials, which increases the resistance of the cell, hinders the conduction of oxygen ions, and ultimately leads to deterioration of cell performance. Therefore, the selection of electrode materials that match the electrolyte is essential for the performance of cells.

In this work, the thermal expansion coefficient, sintering behavior and electrical conductivity of BTM were characterized. The chemical compatibility of different electrode materials (LSC, LSCF, LSM, BCFZY, PBM, SFM, NiO) [25–30] with BTM and the polarization impedance of different materials were investigated by XRD and EIS. In addition, a single cell with Ag|BTM|Ag structure was prepared, and the electrochemical performance of the single cell was tested in the range of 600–800 °C with air as the oxidizer and wet hydrogen (3%  $\text{H}_2\text{O}$ ) as the fuel.

## 2. Experimental

### 2.1. Material Synthesis

The BTM was synthesized using a conventional solid-state reaction method [24].  $\text{BaCO}_3$ ,  $\text{Ta}_2\text{O}_5$ , and  $\text{MoO}_3$  were weighed with the stoichiometric ratio of  $\text{Ba}_7\text{Ta}_{3.7}\text{Mo}_{1.3}\text{O}_{20.15}$  and ball-milled in ethanol for 24 h. After drying and grinding, the mixture was calcined in air at 1000 °C for 10 h, and the calcined powder was granulated by adding 10% polyvinyl alcohol (PVA). The  $(\text{La}_{0.75}\text{Sr}_{0.25})_{0.95}\text{MnO}_{3\pm\delta}$ ,  $\text{La}_{0.6}\text{Sr}_{0.4}\text{CoO}_3$ , and  $\text{La}_{0.6}\text{Sr}_{0.4}\text{Co}_{0.2}\text{Fe}_{0.8}\text{O}_{3+\delta}$  powders were purchased from Ningbo SOFCMAN Energy Technology Co., Ltd., Ningbo, China. The NiO was purchased from Chengdu Shudu Nanomaterials Technology, Chengdu, China.  $\text{PrBaMn}_2\text{O}_{5+\delta}$  was synthesized by a sol-gel method.  $\text{Ba}(\text{NO}_3)_3 \cdot 6\text{H}_2\text{O}$ ,  $\text{Pr}(\text{NO}_3)_3 \cdot 6\text{H}_2\text{O}$ ,  $\text{Mn}(\text{NO}_3)_3 \cdot 9\text{H}_2\text{O}$ , and citric acid were dissolved in deionized water, with stirring and heating the solution to obtain the initial powder, then calcined at 1200 °C for 2 h and reduced in wet hydrogen at 800 °C for 2 h to obtain the final powder. The  $\text{Sr}_2\text{Fe}_{1.5}\text{Mo}_{0.5}\text{O}_{6-\delta}$  powders were prepared in the same procedure as PBM with  $\text{Mo}_7(\text{NH}_4)_6\text{O}_{24} \cdot 4\text{H}_2\text{O}$ ,  $\text{Sr}(\text{NO}_3)_2$ , and  $\text{Fe}(\text{NO}_3)_3 \cdot 9\text{H}_2\text{O}$  as raw materials, and finally calcined at 1100 °C for 5 h.  $\text{BaCo}_{0.4}\text{Fe}_{0.4}\text{Zr}_{0.1}\text{Y}_{0.1}\text{O}_{3-\delta}$  powders were prepared in the same procedure as BTM, with raw materials  $\text{BaCO}_3$ ,  $\text{Co}_2\text{O}_3$ ,  $\text{Fe}_2\text{O}_3$ ,  $\text{ZrO}_2$ , and  $\text{Y}_2\text{O}_3$ ; after that, the initial powders were calcined at 1100 °C for 2 h to obtain the final powders.

### 2.2. Preparation of Symmetric Cells and Single Cells

The BTM powder was pressed into pellets under 10 MPa and then sintered in static air at 1300 °C for 4 h. The BTM pellet was used as the electrolyte of the symmetric cell (diameter of 9 mm, thickness of 0.84 mm). A mixture of electrode powder with ethyl cellulose and terpineol in a 1:1.25 mass ratio was used to obtain the electrode ink. The obtained electrode inks were coated on both sides of the BTM electrolyte pellet and then sintered at 1100 °C for 2 h to obtain a symmetric cell. For the preparation of electrolyte-supported single cells, silver paste was coated on both sides of the electrolyte pellet to prepare a single cell with a Ag|BTM|Ag configuration. Figure 1 shows the schematic diagrams of the preparation of symmetric cells and single cells.

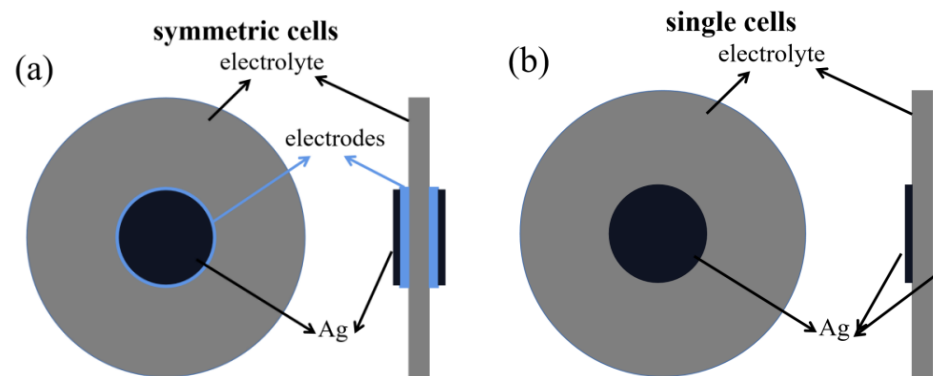


**Figure 1.** Schematic diagrams of the preparation of (a) symmetric cells and (b) single cells.

### 2.3. Characterization

The phase compositions of the BTM powders were analyzed using X-Ray diffraction (XRD) in the  $2\theta$  range of  $20\text{--}80^\circ$ . The density of the BTM electrolyte was measured by the Archimedean water displacement method. The surface of electrolyte particles and electrodes are coated with silver paste, which acts as a current collector, and the electrochemical impedance spectra (EIS) of the cells were measured by an electrochemical workstation (CHI 760e, SCHI) at a bias voltage of 5 mV over a temperature range of  $450\text{--}700^\circ\text{C}$  and a frequency range of 0.1 Hz to 100 kHz. The effective area of the cell's cathode was  $\sim 0.28\text{ cm}^2$ .

## 3. Results and Discussion

### 3.1. Characterization of the $\text{Ba}_7\text{Ta}_{3.7}\text{Mo}_{1.3}\text{O}_{20.15}$ Electrolyte

Figure 2 shows the XRD pattern of the BTM powder calcined at  $1000^\circ\text{C}$  for 10 h. The XRD pattern of BTM is similar to  $\text{Ba}_7\text{Nb}_4\text{MoO}_{20}$ , which suggests the successful synthesis of the hexagonal perovskite structure [23,24]. The lattice parameters of BTM are  $a = b = 5.876\text{ \AA}$  and  $c = 16.589\text{ \AA}$ .

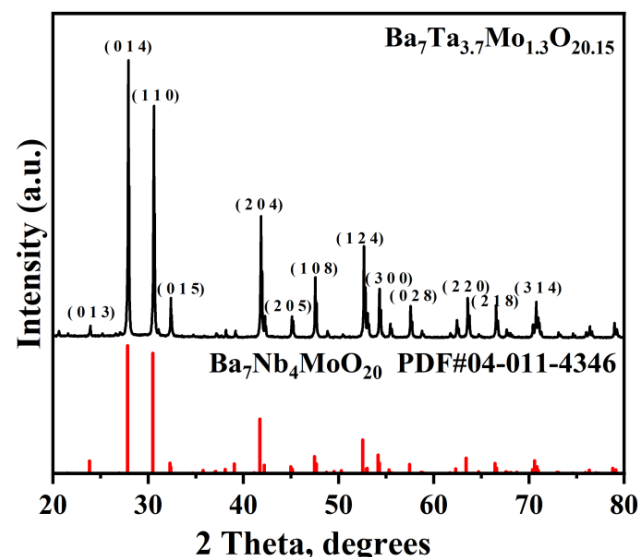


**Figure 2.** XRD pattern of the BTM powder obtained at  $1000^\circ\text{C}$  for 10 h.

In order to optimize the sintering process, the physical and electrical properties of the BTM series samples were investigated in relation to the sintering schedule. The BTM powder was pressed into pellets under 10 MPa, sintered at  $1300^\circ\text{C}$  for 2, 4, 5, 10, and 24 h, and at  $1350^\circ\text{C}$  for 2, 4, 5, and 10 h. The relative density and conductivity of the electrolytes with different sintering schedules are given in Figure 3a. When the sintering temperature

was 1300 °C, the conductivity and density of BTM increased with the soaking time, and the best performance was achieved when the soaking time was 4 h, and then gradually decreased. When the sintering temperature was 1350 °C, the conductivity and bulk density gradually decreased with the increase in soaking time. The highest density and conductivity of the sample were obtained after sintering at 1300 °C for 4 h. The relative density was 94% and the conductivity measured at 600 °C was  $4.5 \times 10^{-3} \text{ S cm}^{-1}$ . Decreased densities at longer soaking times may be attributed to oversintering, which leads to the formation of rapid grain growth and large pores. Furthermore, considering the molybdenum oxide volatilizes at high temperatures, it is reasonable that the conductivity of the BTM electrolyte decreases with increasing temperature and time of sintering. It can be seen from Figure 3b that the density of the electrolyte has a greater effect on the grain boundary conductivity. The grain boundary conductance of dense electrolytes is considerably higher than that of non-dense electrolytes. Figure 3c,d shows the Arrhenius plots of the electrolytes sintered at 1300 °C and 1350 °C, respectively. It is observed that the activation energy decreases with the increase in the electrolyte densities.

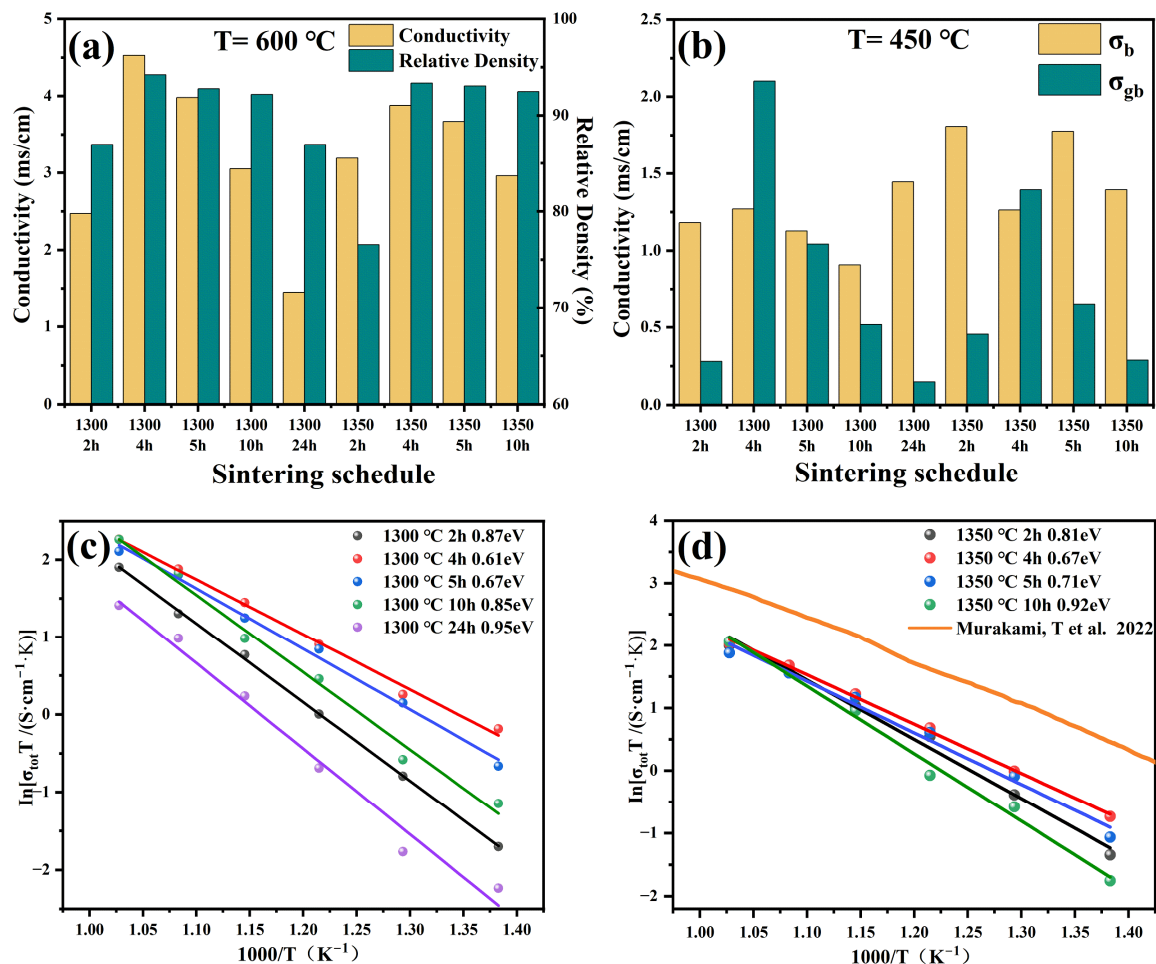


**Figure 3.** (a) Relative densities of electrolytes with different sintering schedules and conductivity measured at 600 °C; (b) bulk and grain boundary conductivities of different electrolytes at 450 °C; (c) Arrhenius plots of electrolytes sintered at 1300 °C; (d) Arrhenius plots of electrolytes sintered at 1350 °C [24].

The SEM images of the cross-section of the electrolyte pellets obtained after sintering at 1300 °C for 4 h are shown in Figure 4. As can be seen in Figure 4a, the electrolytes have a dense microstructure with no obvious pores in the cross-section. It can be noticed from Figure 4c,d that the BTM grains are oblong, which has not been reported before.

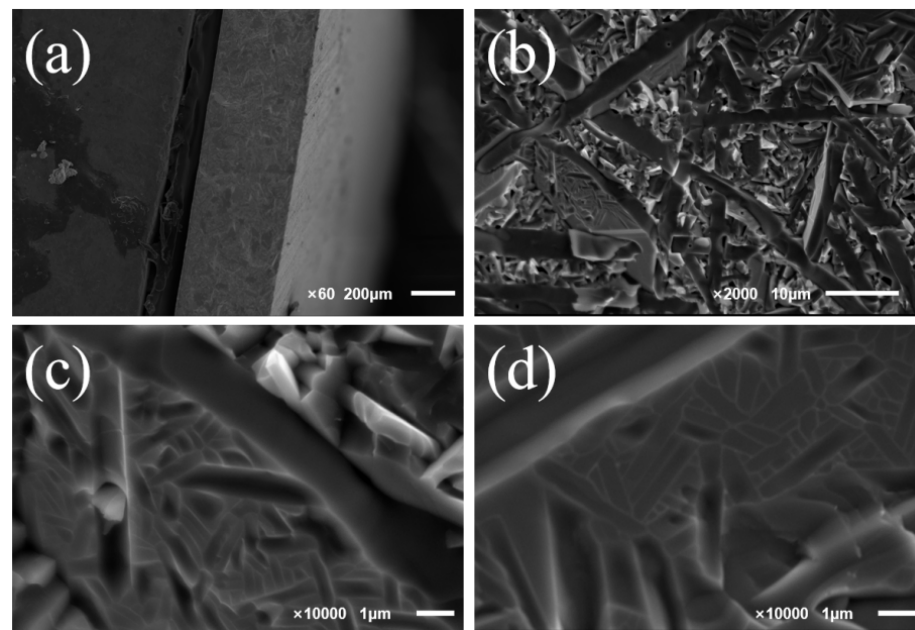


**Figure 4.** The cross-sectional SEM images of the electrolyte pellets obtained after sintering at 1300 °C for 4 h, (a) magnification  $\times 60$ ; (b) magnification  $\times 2000$ ; (c) magnification  $\times 10,000$ ; (d) magnification  $\times 10,000$ .

Figure 5 shows the thermal expansion curve (TEC) of BTM, and the TEC (20–800 °C) of BTM is  $14.1 \times 10^{-6} \text{ K}^{-1}$ , which is compatible with most electrode materials ( $15.3 \times 10^{-6} \text{ K}^{-1}$  for LSCF,  $17.2 \times 10^{-6} \text{ K}^{-1}$  for BCFZY,  $14.9 \times 10^{-6} \text{ K}^{-1}$  for SFM,  $20.5 \times 10^{-6} \text{ K}^{-1}$  for LSC,  $14.1 \times 10^{-6} \text{ K}^{-1}$  for NiO) [31–34].

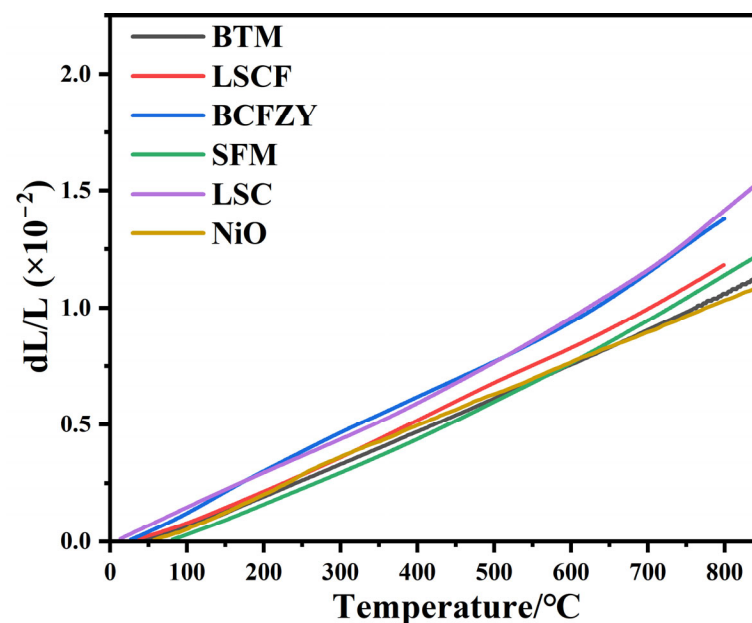


**Figure 5.** The thermal expansion curves of different materials.

### 3.2. Chemical Compatibility of $Ba_7Ta_{3.7}Mo_{1.3}O_{20.15}$ with Different Electrodes

The reaction between the electrolyte and the electrode layer is an important issue to be considered when building SOFCs. Considering the variety of electrode materials, several typical electrode materials have been selected to investigate the compatibility with BTM: (a) LSM, which has been studied intensively as the first-generation cathode

material, in this work, was examined firstly; (b) Among the developed SOFC electrode materials, Co-based electrode materials have been widely studied for their high mixed conductivity. From the viewpoint of thermal expansion and chemical components, the chemical compatibilities of LSC, LSCF, and BCFZY with BTM were tested; (c) Since the anode is the site of fuel conversion, the compatibility between the anode material and the electrolyte is also essential. The chemical compatibility of BTM with the conventional anode material NiO as well as the perovskite anode materials PBM and SFM were studied.

### 3.2.1. LSM Electrode

Figure 6 shows the XRD pattern of the mixture of BTM and LSM after high-temperature heat treatment. It can be seen from the diffraction pattern that the BTM phase has completely disappeared, while the LSM phase still remained. Several other substances were also observed in the diffraction pattern, which were identified as  $\text{BaLa}_{0.5}\text{Ta}_{0.5}\text{O}_3$ ,  $\text{BaLa}_{0.33}\text{TaO}_4$ ,  $\text{BaLa}_{0.7}\text{Mn}_{0.3}\text{O}_3$ ,  $\text{BaMoO}_4$ , and  $\text{Ba}_5\text{Ta}_4\text{O}_{15}$ . This indicates the high reactivity between BTM and LSM.

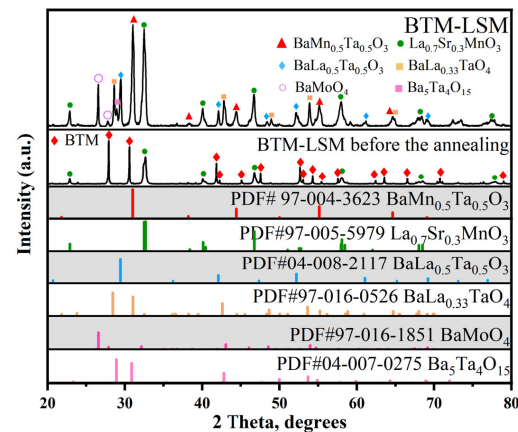


**Figure 6.** XRD pattern of BTM-LSM mixture (1:1 *w/w*) obtained after firing at 1100 °C for 2 h in air.

### 3.2.2. LSC, LSCF, BCFZY Electrodes

The XRD patterns of the mixture of BTM and LSC after high-temperature heat treatment are shown in Figure 7a. It can be observed that the main phase shows a perovskite structure and the BTM phase disappears, but the LSC phase still exists, and an impurity phase is indexed to  $\text{La}_{1.25}\text{Sr}_{0.75}\text{CoO}_4$  [35]. According to the ICDD database, the main phase peaks can be indexed to  $\text{Ba}_2\text{MoCoO}_6$ , and considering that these phases do not contain Ta elements, it is suggested that Ta ions might be doped into the lattice. These results show a high reactivity between BTM and LSC.

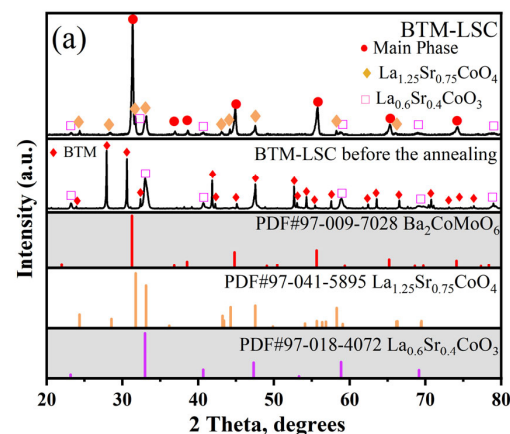


**Figure 7.** Cont.

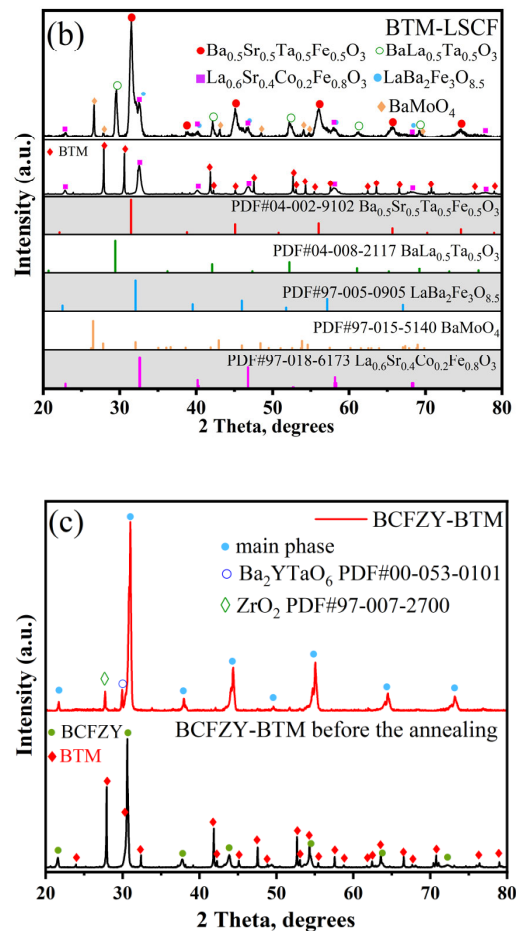


**Figure 7.** (a) XRD pattern of BTM-LSC mixture (1:1 *w/w*) obtained after firing at 1100 °C for 2 h in air; (b) XRD pattern of BTM-LSCF mixture (1:1 *w/w*) obtained after firing at 1100 °C for 2 h in air; (c) XRD pattern of BTM-BCFZY mixture (1:1 *w/w*) obtained after firing at 1100 °C for 2 h in air.

The XRD patterns of the mixture of BTM and LSCF after high-temperature heat treatment are shown in Figure 7b. It can be seen from the diffraction pattern that the BTM phase has completely disappeared, while the LSCF phase still exists. Several other phases were also observed in the diffraction pattern, which were identified as the following possible substances:  $\text{Ba}_{0.5}\text{Sr}_{0.5}\text{Ta}_{0.5}\text{Fe}_{0.5}\text{O}_3$ ,  $\text{BaLa}_{0.5}\text{Ta}_{0.5}\text{O}_3$ ,  $\text{LaBa}_2\text{Fe}_3\text{O}_{8.5}$ , and  $\text{BaMoO}_4$ . This indicates poor compatibility between BTM and LSCF.

The XRD patterns of the mixture of BTM and BCFZY after high-temperature heat treatment are shown in Figure 7c. It is observed that the main diffraction peaks of the calcined mixture are similar to those of BCFZY, and the diffraction peaks of the mixture slightly shift to the high diffraction direction, which might suggest the doping of Ta ions and Mo ions into the lattice. In addition, two small diffraction peaks were observed near 27.7° and 29.9°, which were identified as  $\text{ZrO}_2$  and  $\text{Ba}_3\text{YFe}_2\text{O}_{7.5}$ , respectively.

### 3.2.3. NiO, PBM, SFM Anodes

Figure 8a shows the XRD pattern of the mixture of BTM and NiO after high-temperature heat treatment. It can be observed that the BTM diffraction peaks have disappeared. Three substances are present in the diffraction pattern and are identified as  $\text{BaTa}_{0.67}\text{Ni}_{0.33}\text{O}_3$ , NiO, and  $\text{BaMoO}_4$ . This result indicates the high reactivity between BTM and NiO.

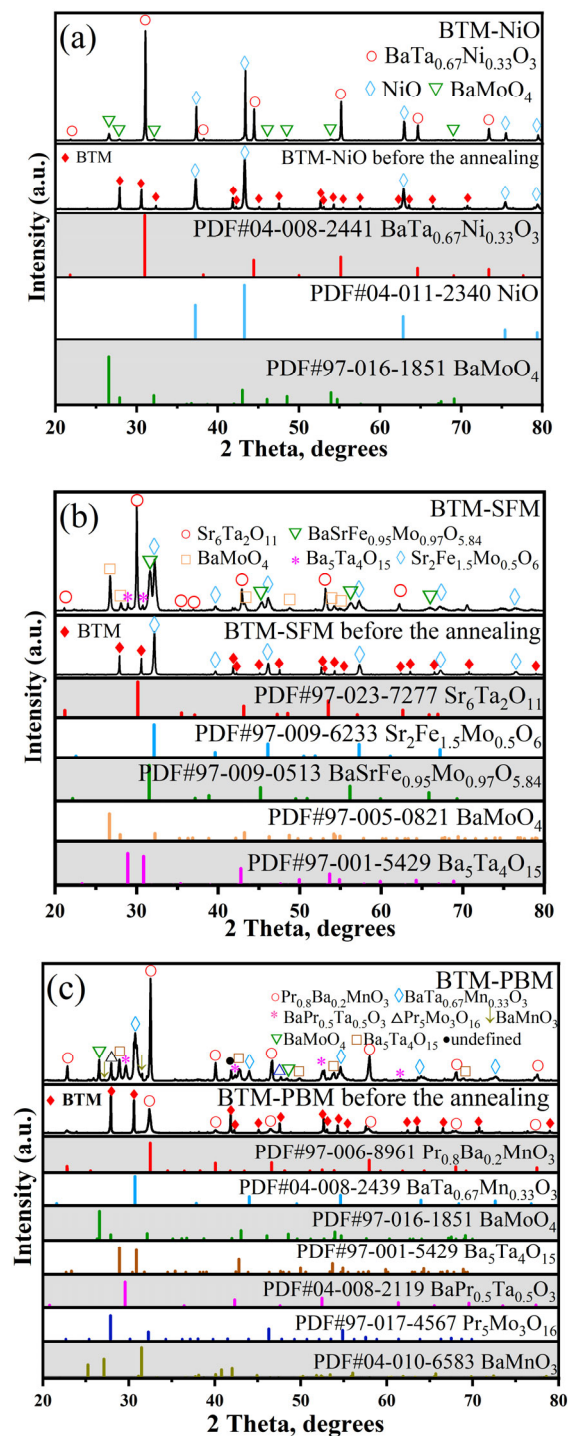


**Figure 8.** (a) XRD pattern of BTM-NiO mixture (1:1 *w/w*) obtained after firing at 1100 °C for 2 h in air; (b) XRD pattern of BTM-SFM mixture (1:1 *w/w*) obtained after firing at 1100 °C for 2 h in air; (c) XRD pattern of BTM-PBM mixture (1:1 *w/w*) obtained after firing at 1100 °C for 2 h in air.

Figure 8b shows the XRD patterns of the mixture of BTM and SFM after high-temperature heat treatment. It is noted that the BTM phase has disappeared, while the SFM phase is still present. Several other substances were also observed in the diffraction pattern, which were identified as  $\text{Sr}_6\text{Ta}_2\text{O}_{11}$ ,  $\text{Ba}_5\text{Ta}_4\text{O}_{15}$ ,  $\text{BaSrFe}_{0.95}\text{Mo}_{0.97}\text{O}_{5.84}$ , and  $\text{BaMoO}_4$ . This result implies high reactivity between BTM and SFM. In particular, Mo readily reacts with alkaline earth metal elements, its high reactivity is also observed for other molybdenum-containing materials [27,28].

Figure 8c shows the XRD patterns of BTM and PBM mixture calcined at 1100 °C. It can be seen that the BTM phase has disappeared, while the PBM phase is still present. Several other substances were also detected in the diffraction pattern, which were identified as  $\text{BaTa}_{0.67}\text{Mn}_{0.33}\text{O}_3$ ,  $\text{Pr}_5\text{Mo}_3\text{O}_{16}$ ,  $\text{BaPr}_{0.5}\text{Ta}_{0.5}\text{O}_3$ ,  $\text{Ba}_5\text{Ta}_4\text{O}_{15}$ ,  $\text{BaMoO}_4$ , and  $\text{BaMnO}_3$ . This result suggests high reactivity between BTM and PBM.

In addition, the chemical compatibility of these electrodes with BTM after calcination at 900 °C was investigated, and the results showed that the chemical compatibility of these electrodes with BTM was still poor at relatively low temperatures (Figure S1).

In summary, the XRD analysis results showed low chemical stability between BTM and most electrode materials. Several commonalities in the chemical reactions between BTM and the electrode materials were found:

- After the chemical reaction, the BTM phase usually disappeared completely while the electrode phase remained, more or less;
- BTM may easily react with oxides containing La, Co, Sr, Ni, Mn, Pr, and Fe elements to form new compounds. Unfortunately, most known efficient electrodes, namely mixed ionic-electronic conductor (MIEC), more or less, contain these elements [1,36–45].

### 3.3. Chemical Stability Analysis

The excellent stability of the electrolyte at high-temperatures is important for SOFC, particularly in the presence of water. The excellent stability of BTM in  $\text{H}_2$  has been confirmed [24]. Considering that some Ba-containing electrolytes may precipitate a second phase after soaking in boiling water, the chemical stability of BTM particles in boiling water was tested. The electrolyte pellets were soaked in boiling water at 100 °C for 3 h, and after that, both sides were coated with silver paste for EIS tests and ground into powder for XRD analysis and the results are shown in Figure 9. The XRD pattern shows no significant change in BTM diffraction peaks before and after the water stability test. The EIS spectra showed a significant increase in the ohmic and grain boundary impedance of the electrolyte after the water stability test, which may be due to the generation of a small amount of a second phase on the electrolyte surface. However, the second phase does not appear in the XRD pattern, which may be due to the amount of the second phase being relatively small and exceeding the detection limit of the machine. The pH of the solution increased from 8 to 10 after the water stability test, which proved the poor stability of BTM in high-temperature environments with enriched water.

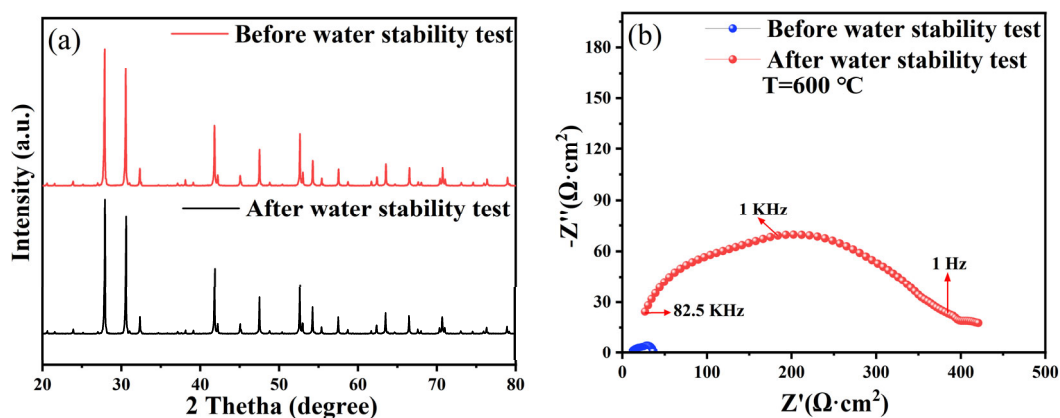


**Figure 9.** (a) XRD patterns of BTM before and after being boiled in water; (b) EIS curve of BTM pellets before and after being boiled in water.

### 3.4. Electrochemical Impedance Spectroscopy Analysis

Figure 10a,b shows EIS plots of BTM-based symmetric cells with different electrodes. These electrode materials exhibit particularly poor electrochemical properties. The  $R_{\Gamma}(R_1Q_1)(R_2Q_2)$  equivalent circuit model is used to fit the impedance spectrum,  $R\Omega$

is the ohmic resistance of the electrolyte and ( $RQ$ ) corresponds to the different electrode processes. The polarization impedance  $R_p$  is the sum of the impedances corresponding to the electrode processes. The polarization impedance values are summarized in Table 1.

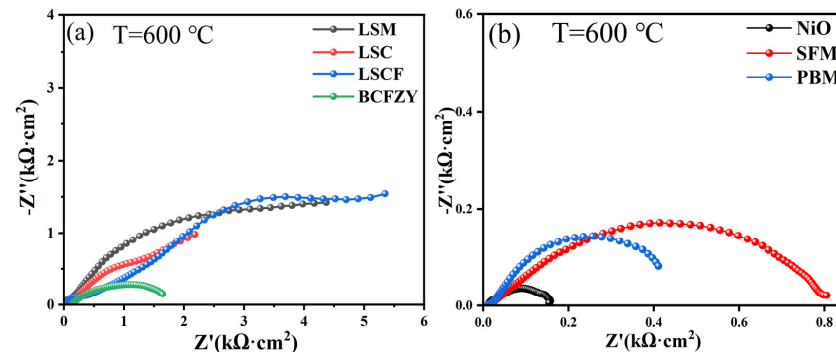


**Figure 10.** EIS plot of “electrode | BTM | electrode” symmetric cell measured at 600 °C: (a) LSM, LSC, LSCF, BCFZY electrodes measured in wet air; (b) NiO, SFM, PBM electrodes measured in wet  $H_2$ .

**Table 1.** Polarization impedance values of these electrodes.

Electrode	LSM	LSC	LSCF	BCFZY	NiO	SFM	PBM
Polarization impedance ( $k\Omega \cdot cm^{-2}$ )	>4.26	>2.15	>5.31	~1.49	~0.14	~0.78	~0.4

As shown in Table 1, the highest polarization impedance of these electrodes is more than  $5.31 k\Omega \cdot cm^{-2}$  and the lowest is  $0.14 k\Omega \cdot cm^{-2}$ . These poor electrochemical performances could be attributed to the aforementioned chemical reactions between BTM and the electrode materials. However, for the electrode of intermediate temperature solid oxide fuel cells, the acceptable ASR values usually do not exceed  $1 \Omega \cdot cm^{-2}$ . Therefore, the strong chemical reaction between BTM and common MIEC electrodes seriously hinders the application of the BTM electrolyte.

Figure 11 shows the EIS curve of the Ag | BTM | Ag symmetric cell measured in air at 600 °C. The polarization impedance of silver as an electrode is  $10.24 \Omega \cdot cm^2$ . Although silver electrode is still far from offering acceptable performance, it exhibits a relatively low impedance value compared to other electrode materials due to the chemical inertness of silver. In addition, Ag | BTM | Ag single cells were prepared with an open circuit voltage of 1.05 V at 800 °C (Figure S2). This value is close to the theoretical value calculated from the Nernst equation, demonstrating that there is negligible electronic conductivity and few flaws (cracks, pinholes, etc.) in the BTM electrolyte.

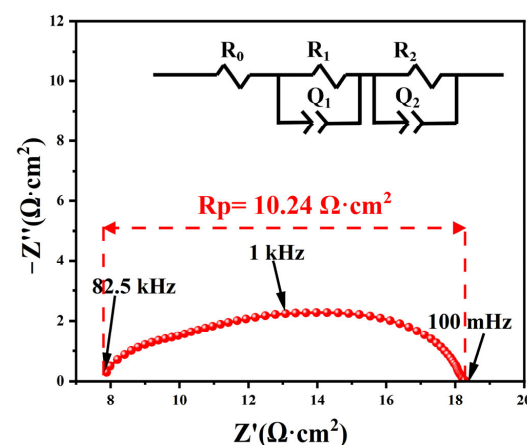


**Figure 11.** EIS curve of Ag | BTM | Ag symmetric cell.

#### 4. Conclusions

In this paper, the  $\text{Ba}_7\text{Ta}_{3.7}\text{Mo}_{1.3}\text{O}_{20.15}$  electrolyte was prepared by a solid-state reaction. We optimized the sintering regime for BTM, and the conductivity reaches  $4.5 \times 10^{-3} \text{ S cm}^{-1}$  when sintered at  $1300 \text{ }^\circ\text{C}$  for 4 h. The thermal expansion coefficient of BTM was reported for the first time and the average thermal expansion coefficient of BTM is measured as  $14.1 \times 10^{-6} \text{ K}^{-1}$  in the temperature range from 20 to  $800 \text{ }^\circ\text{C}$ . The compatibility of LSM, LSC, LSCF, BCFZY, NiO, SFM, and PBM electrode materials with BTM electrolyte was investigated. Unfortunately, the results of XRD analysis suggested that BTM is very prone to react with electrodes containing La, Co, Sr, Ni, Mn, and Fe elements at high temperatures to form resistive phases and, consequently, result in poor electrochemical performance. This result revealed the high reactivity between BTM and commonly used electrode materials for the first time. Silver, as an electrode, exhibits relatively lower polarization impedance compared to the above materials. Therefore, due to the fact that BTM is not compatible with most known SOFC electrode materials, further research is urgently needed to develop new effective electrodes compatible with BTM or new strategies to alleviate the chemical reactions between BTM and electrodes.

**Supplementary Materials:** The following supporting information can be downloaded at: <https://www.mdpi.com/article/10.3390/ma16113919/s1>. Figure S1: XRD patterns of different materials after firing at  $900 \text{ }^\circ\text{C}$  for 2 h in air, (a) BTM-LSM mixture (1:1 w/w); (b) BTM-LSC mixture (1:1 w/w); (c) BTM-LSCF mixture (1:1 w/w); (d) BTM-BCFZY mixture (1:1 w/w); (e) BTM-NiO mixture (1:1 w/w); (f) BTM-SFM mixture (1:1 w/w); (g) BTM-PBM mixture (1:1 w/w). Figure S2: V-I and P-I curves of Ag|BTM|Ag cell.

**Author Contributions:** Investigation, D.X., X.Z., Y.L., X.Y., Z.Y. and Y.M.; writing—original draft preparation, D.X.; formal analysis, D.X., X.Y., Y.L., Z.Y. and B.S.; methodology, D.X., Y.L. and X.Z.; data curation, X.Z.; writing—review and edit, B.S., B.W. and L.G.; validation, Y.M. and B.W.; conceptualization, L.G.; funding acquisition, L.G. All authors have read and agreed to the published version of the manuscript.

**Funding:** This work was supported by National Natural Science Foundation of China (No. 51502136 and No. 21978133), the Natural Science Foundation of Jiangsu Province (BK 20211260), the Priority Academic Program Development (PAPD) of Jiangsu Higher Education Institutions and Top-notch Academic Programs Project of Jiangsu Higher Education Institutions (TAPP).

**Institutional Review Board Statement:** Not applicable.

**Informed Consent Statement:** Not applicable.

**Data Availability Statement:** All data is available from the corresponding author.

**Acknowledgments:** We are grateful to Yifeng Zheng and Han Chen for providing all the facilities and raw materials.

**Conflicts of Interest:** The authors declare that they have no competing interest.

#### References

1. Xu, Y.; Xu, X.; Bi, L. A high-entropy spinel ceramic oxide as the cathode for proton-conducting solid oxide fuel cells. *J. Adv. Ceram.* **2022**, *11*, 794–804. [[CrossRef](#)]
2. Han, D.L.; Uda, T. The best composition of an Y-doped  $\text{BaZrO}_3$  electrolyte: Selection criteria from transport properties, microstructure, and phase behavior. *J. Mater. Chem. A* **2018**, *6*, 18571–18582.
3. Bauerle, J.E. Study of solid electrolyte polarization by a complex admittance method. *J. Phys. Chem. Solids* **1969**, *30*, 2657–2670. [[CrossRef](#)]
4. Suemoto, T.; Ishigame, M. Composition dependence of the ionic diffusion coefficients in yttria-stabilized zirconias. *Solid State Ion.* **1986**, *21*, 225–229. [[CrossRef](#)]
5. Ge, L.; Guo, K.; Guo, L. Sinterability, reducibility, and electrical conductivity of fast oxide-ion conductors  $\text{La}_{1.8}\text{R}_{0.2}\text{MoWO}_9$  (R = Pr, Nd, Gd and Y). *Ceram. Int.* **2015**, *41*, 10208–10215. [[CrossRef](#)]
6. Pergolesi, D.; Fabbri, E.; D'Epifanio, A.; Di Bartolomeo, E.; Tebano, A.; Sanna, S.; Licoccia, S.; Balestrino, G.; Traversa, E. High proton conduction in grain-boundary-free yttrium-doped barium zirconate films grown by pulsed laser deposition. *Nat. Mater.* **2010**, *9*, 846–852. [[CrossRef](#)] [[PubMed](#)]

7. Kreuer, K.D. Proton-conducting oxides. *Annu. Rev. Mater.* **2003**, *33*, 333–359. [[CrossRef](#)]
8. Bi, L.; Fang, S.M.; Tao, Z.T.; Zhang, S.Q.; Peng, R.R.; Liu, W. Influence of anode pore forming additives on the densification of supported BaCe<sub>0.7</sub>Ta<sub>0.1</sub>Y<sub>0.2</sub>O<sub>3-δ</sub> electrolyte membranes based on a solid state reaction. *J. Eur. Ceram. Soc.* **2009**, *29*, 2567–2573. [[CrossRef](#)]
9. Ge, L.; Jiao, J.; Zhu, Z.; Zhang, Q.; Zheng, Y.; Chen, H.; Guo, L. A facile method to fabricate proton-conducting BaZr<sub>0.85</sub>Y<sub>0.15</sub>O<sub>3-δ</sub> electrolyte with a large grain size and high conductivity. *Ceram. Int.* **2019**, *45*, 24946–24952. [[CrossRef](#)]
10. Jiao, J.; Li, Q.; Gu, Y.; Luo, Y.; Ge, L.; Zheng, Y.; Chen, H.; Guo, L. Effect of BaO-B<sub>2</sub>O<sub>3</sub> composite sintering aid on sinterability and electrical property of BaZr<sub>0.85</sub>Y<sub>0.15</sub>O<sub>3-δ</sub> ceramic. *Ceram. Int.* **2019**, *45*, 13679–13684. [[CrossRef](#)]
11. Kuang, X.; Green, M.A.; Niu, H.; Zajdel, P.; Dickinson, C.; Claridge, J.B.; Jantsky, L.; Rosseinsky, M.J. Interstitial oxide ion conductivity in the layered tetrahedral network melilite structure. *Nat. Mater.* **2008**, *7*, 498–504. [[CrossRef](#)] [[PubMed](#)]
12. Marrero-Lopez, D.; Martin-Sedeno, M.C.; Pena-Martinez, J.; Ruiz-Morales, J.C.; Nunez, P.; Aranda, M.A.G.; Ramos-Barrado, J.R. Evaluation of apatite silicates as solid oxide fuel cell electrolytes. *J. Power Sources* **2010**, *195*, 2496–2506. [[CrossRef](#)]
13. Shi, H.G.; Su, C.; Ran, R.; Cao, J.F.; Shao, Z.P. Electrolyte materials for intermediate-temperature solid oxide fuel cells. *Prog. Nat. Sci.* **2020**, *30*, 764–774. [[CrossRef](#)]
14. Singh, K.; Kannan, R.; Thangadurai, V. Perspective of perovskite-type oxides for proton conducting solid oxide fuel cells. *Solid State Ion.* **2019**, *339*, 13. [[CrossRef](#)]
15. Rajendran, S.; Thangavel, N.K.; Alkatie, S.; Ding, Y.; Arava, L.M.R. Y, Gd, and Pr tri-doped perovskite-type proton conducting electrolytes with improved sinterability and chemical stability. *J. Alloys Compd.* **2021**, *870*, 7. [[CrossRef](#)]
16. Fukui, T.; Ohara, S.; Murata, K.; Yoshida, H.; Miura, K.; Inagaki, T. Performance of intermediate temperature solid oxide fuel cells with La(Sr)Ga(Mg)O<sub>3</sub> electrolyte film. *J. Power Sources* **2002**, *106*, 142–145. [[CrossRef](#)]
17. Ishihara, T.; Matsuda, H.; Takita, Y. Doped LaGaO<sub>3</sub> perovskite type oxide as a new oxide ionic conductor. *J. Am. Chem. Soc.* **1994**, *116*, 3801–3803. [[CrossRef](#)]
18. Iwahara, H.; Uchida, H.; Ono, K.; Ogaki, K. Proton conduction in sintered oxides based on BaCeO<sub>3</sub>. *J. Electrochem. Soc.* **1988**, *135*, 529–533. [[CrossRef](#)]
19. Wienstroer, S.; Wiemhofer, H.D. Investigation of the influence of zirconium substitution on the properties of neodymium-doped barium cerates. *Solid State Ion.* **1997**, *101*, 1113–1117. [[CrossRef](#)]
20. Fop, S.; McCombie, K.S.; Wildman, E.J.; Skakle, J.M.S.; Irvine, J.T.S.; Connor, P.A.; Savaniu, C.; Ritter, C.; McLaughlin, A.C. High oxide ion and proton conductivity in a disordered hexagonal perovskite. *Nat. Mater.* **2020**, *19*, 752–757. [[CrossRef](#)]
21. Nguyen, L.T.; Cava, R.J. Hexagonal Perovskites as Quantum Materials. *Chem. Rev.* **2021**, *121*, 2935–2965. [[CrossRef](#)] [[PubMed](#)]
22. Yashima, M.; Tsujiguchi, T.; Sakuda, Y.; Yasui, Y.; Zhou, Y.; Fujii, K.; Torii, S.; Kamiyama, T.; Skinner, S.J. High oxide-ion conductivity through the interstitial oxygen site in Ba<sub>7</sub>Nb<sub>4</sub>MoO<sub>20</sub>-based hexagonal perovskite related oxides. *Nat. Commun.* **2021**, *12*, 7. [[CrossRef](#)] [[PubMed](#)]
23. Suzuki, Y.; Murakami, T.; Fujii, K.; Hester, J.R.; Yasui, Y.; Yashima, M. Simultaneous Reduction of Proton Conductivity and Enhancement of Oxide-Ion Conductivity by Aliovalent Doping in Ba<sub>7</sub>Nb<sub>4</sub>MoO<sub>20</sub>. *Inorg. Chem.* **2022**, *61*, 7537–7545. [[CrossRef](#)] [[PubMed](#)]
24. Murakami, T.; Shibata, T.; Yasui, Y.; Fujii, K.; Hester, J.R.; Yashima, M. High Oxide-Ion Conductivity in a Hexagonal Perovskite-Related Oxide Ba<sub>7</sub>Ta<sub>3.7</sub>Mo<sub>1.3</sub>O<sub>20.15</sub> with Cation Site Preference and Interstitial Oxide Ions. *Small* **2022**, *18*, 8. [[CrossRef](#)] [[PubMed](#)]
25. Zhang, L.L.; Yin, Y.R.; Xu, Y.S.; Yu, S.F.; Bi, L. Tailoring Sr<sub>2</sub>Fe<sub>1.5</sub>Mo<sub>0.5</sub>O<sub>6-δ</sub> with Sc as a new single-phase cathode for proton-conducting solid oxide fuel cells. *Sci. China Mater.* **2022**, *65*, 1485–1494. [[CrossRef](#)]
26. Kim, H.; Ida, S.; Ju, Y.W.; Matsuda, J.; Kim, G.; Ishihara, T. Mixing effects of Cr<sub>2</sub>O<sub>3</sub>-PrBaMn<sub>2</sub>O<sub>5</sub> for increased redox cycling properties of Fe powder for a solid-oxide Fe-air rechargeable battery. *J. Mater. Chem. A* **2017**, *5*, 364–371. [[CrossRef](#)]
27. Wei, K.; Li, N.; Wu, Y.; Song, W.; Wang, X.; Guo, L.; Khan, M.; Wang, S.; Zhou, F.; Ling, Y. Characterization and optimization of highly active and Ba-deficient BaCo<sub>0.4</sub>Fe<sub>0.4</sub>Zr<sub>0.1</sub>Y<sub>0.1</sub>O<sub>3-δ</sub>-based cathode materials for protonic ceramics fuel cells. *Ceram. Int.* **2019**, *45*, 18583–18591. [[CrossRef](#)]
28. Zhu, Z.; Sun, K.; Xu, D.; Gu, Y.; Ni, Q.; Zheng, Y.; Chen, H.; Ge, L.; Huang, X.; Guo, L. Enhancing the performance of symmetrical solid oxide fuel cells with Sr<sub>2</sub>Fe<sub>1.5</sub>Mo<sub>0.5</sub>O<sub>6-δ</sub> electrodes via infiltration of Pr<sub>6</sub>O<sub>11</sub> bifunctional catalyst. *Electrochim. Acta* **2022**, *402*, 139569. [[CrossRef](#)]
29. Gu, Y.; Zhang, Y.; Zheng, Y.; Chen, H.; Ge, L.; Guo, L. PrBaMn<sub>2</sub>O<sub>5+δ</sub> with praseodymium oxide nano-catalyst as electrode for symmetrical solid oxide fuel cells. *Appl. Catal. B Environ.* **2019**, *257*, 117868. [[CrossRef](#)]
30. Ge, L.; Sun, K.; Gu, Y.; Ni, Q.; Huang, X. Boosting the performance of conventional air electrodes for solid oxide cells by in-situ loading of nano praseodymium oxide. *Energy Convers. Manag.* **2021**, *249*, 114873. [[CrossRef](#)]
31. Kostogloudis, G.C.; Ftikos, C. Properties of A-site-deficient La<sub>0.6</sub>Sr<sub>0.4</sub>Co<sub>0.2</sub>Fe<sub>0.8</sub>O<sub>3-δ</sub>-based perovskite oxides. *Solid State Ion.* **1999**, *126*, 143–151. [[CrossRef](#)]
32. Wang, W.; Zhang, X.Z.; Khan, K.; Wu, H.D.; Zhang, D.D.; Yang, Y.; Jiang, Y.H.; Lin, B. Enhanced ORR activity of A-site deficiency engineered BaCo<sub>0.4</sub>Fe<sub>0.4</sub>Zr<sub>0.1</sub>Y<sub>0.1</sub>O<sub>3-δ</sub> cathode in practical YSZ fuel cells. *Int. J. Hydrogen Energy* **2021**, *46*, 5593–5603. [[CrossRef](#)]
33. Hou, M.Y.; Sun, W.; Li, P.F.; Feng, J.; Yang, G.Q.; Qiao, J.S.; Wang, Z.H.; Rooney, D.; Feng, J.S.; Sun, K.N. Investigation into the effect of molybdenum-site substitution on the performance of Sr<sub>2</sub>Fe<sub>1.5</sub>Mo<sub>0.5</sub>O<sub>6-δ</sub> for intermediate temperature solid oxide fuel cells. *J. Power Sources* **2014**, *272*, 759–765. [[CrossRef](#)]

34. Huang, K.Q.; Goodenough, J.B. Oxygen permeation through cobalt-containing perovskites—Surface oxygen exchange vs. lattice oxygen diffusion. *J. Electrochem. Soc.* **2001**, *148*, E203–E214. [[CrossRef](#)]
35. Marrero-Lopez, D.; Pena-Martinez, J.; Ruiz-Morales, J.C.; Perez-Coll, D.; Martin-Sedeno, M.C.; Nunez, P. Applicability of  $\text{La}_2\text{Mo}_{2-y}\text{W}_y\text{O}_9$  materials as solid electrolyte for SOFCs. *Solid State Ion.* **2007**, *178*, 1366–1378. [[CrossRef](#)]
36. Zhu, Z.; Gong, Z.; Qu, P.; Li, Z.; Rasaki, S.A.; Liu, Z.; Wang, P.; Liu, C.; Lao, C.; Chen, Z. Additive manufacturing of thin electrolyte layers via inkjet printing of highly-stable ceramic inks. *J. Adv. Ceram.* **2021**, *10*, 279–290. [[CrossRef](#)]
37. Li, P.; Yang, W.; Tian, C.; Zhao, W.; Lu, Z.; Xie, Z.; Wang, C.-A. Electrochemical performance of  $\text{La}_2\text{NiO}_{4+\delta}\text{-Ce}_{0.55}\text{La}_{0.45}\text{O}_{2-\delta}$  as a promising bifunctional oxygen electrode for reversible solid oxide cells. *J. Adv. Ceram.* **2021**, *10*, 328–337. [[CrossRef](#)]
38. Ling, Y.; Guo, T.; Guo, Y.; Yang, Y.; Tian, Y.; Wang, X.; Ou, X.; Feng, P. New two-layer Ruddlesden-Popper cathode materials for protonic ceramics fuel cells. *J. Adv. Ceram.* **2021**, *10*, 1052–1060. [[CrossRef](#)]
39. Zvonareva, I.A.; Mineev, A.M.; Tarasova, N.A.; Fu, X.-Z.; Medvedev, D.A. High-temperature transport properties of  $\text{BaSn}_{1-x}\text{Sc}_x\text{O}_{3-\delta}$  ceramic materials as promising electrolytes for protonic ceramic fuel cells. *J. Adv. Ceram.* **2022**, *11*, 1131–1143. [[CrossRef](#)]
40. Xiong, D.; Rasaki, S.A.; Li, Y.; Fan, L.; Liu, C.; Chen, Z. Enhanced cathodic activity by tantalum inclusion at B-site of  $\text{La}_{0.6}\text{Sr}_{0.4}\text{Co}_{0.4}\text{Fe}_{0.6}\text{O}_3$  based on structural property tailored via camphor-assisted solid-state reaction. *J. Adv. Ceram.* **2022**, *11*, 1330–1342. [[CrossRef](#)]
41. Xu, Y.; Yu, S.; Yin, Y.; Bi, L. Taking advantage of Li-evaporation in  $\text{LiCoO}_2$  as cathode for proton-conducting solid oxide fuel cells. *J. Adv. Ceram.* **2022**, *11*, 1849–1859. [[CrossRef](#)]
42. Luo, J.; Zhao, K.; Zhao, J.; Li, J.; Liu, Y.; Chen, D.; Xu, Q.; Chen, M. Functional ceramic support as an independent catalyst layer for direct liquid fuel solid oxide fuel cells. *J. Adv. Ceram.* **2023**, *12*, 474–486. [[CrossRef](#)]
43. Yin, Y.R.; Zhou, Y.B.; Gu, Y.Y.; Bi, L. Successful preparation of  $\text{BaCo}_{0.5}\text{Fe}_{0.5}\text{O}_{3-\delta}$  cathode oxide by rapidly cooling allowing for high-performance proton-conducting solid oxide fuel cells. *J. Adv. Ceram.* **2023**, *12*, 587–597. [[CrossRef](#)]
44. Qiu, P.; Liu, B.; Wu, L.; Qi, H.; Tu, B.; Li, J.; Jia, L. K-doped  $\text{BaCo}_{0.4}\text{Fe}_{0.4}\text{Zr}_{0.2}\text{O}_{3-\delta}$  as a promising cathode material for protonic ceramic fuel cells. *J. Adv. Ceram.* **2022**, *11*, 1988–2000. [[CrossRef](#)]
45. Li, Z.; Yang, B.; Qian, B.; Wang, S.; Zheng, Y.; Ge, L.; Chen, H. Evaluation of Fe-doped  $\text{Pr}_{1.8}\text{Ba}_{0.2}\text{NiO}_4$  as a high-performance air electrode for reversible solid oxide cell. *Sep. Purif. Technol.* **2023**, *308*, 123002. [[CrossRef](#)]

**Disclaimer/Publisher’s Note:** The statements, opinions and data contained in all publications are solely those of the individual author(s) and contributor(s) and not of MDPI and/or the editor(s). MDPI and/or the editor(s) disclaim responsibility for any injury to people or property resulting from any ideas, methods, instructions or products referred to in the content.